Modeling, Modulation, and Control of the Three-Phase Four-Switch PWM Rectifier Under Balanced Voltage

Zhiyong Zeng, Weiyi Zheng, Rongxiang Zhao, Chong Zhu, and Qingwei Yuan

***Abstract*—The modeling, modulation, and control of the three-phase four-switch (TPFS) PWM rectifier are investigated in this paper. Three space vector pulse width modulation methods using different equivalent zero vectors are developed, where sector identification and the trigonometric function are not required. Then, the high-frequency model for the current ripple analysis is proposed, and the effects of three SVM approaches on the ac current ripple are investigated. According to the analytical results, the method introducing the smallest current ripple is selected. With the optimized SVM approach, a control-oriented model, considering the capacitor voltage oscillation and deviation, is built in the *dq* synchronous frame to facilitate the controller design. Furthermore, a control strategy implementing the proportional controller is developed to eliminate the capacitor voltage deviation. Meanwhile, the dual-loop control of the TPFS is not affected by the proposed strategy as the capacitor voltage deviation is eliminated. Finally, a novel linear modulation index function is defined to reject the low-frequency harmonic current introduced by the overmodulation. Experimental results demonstrate that excellent current performance is achieved with comprehensive considerations of the modeling, modulation, and control strategy.**

***Index Terms*—AC–DC power rectifiers, current ripple root mean square (RMS), linear modulation, space vector modulation (SVM), three-phase four-switch (TPFS).**

I. Introduction

THE three-phase six-switch (TPSS) PWM boost rectifier is widely implemented as a utility interface with renewable energy resources in the fields of solar energy, wind energy, active power filter, and unified power flow control [1]–[7]. Due to cost and reliability considerations, research efforts have been made to develop power semiconductor devices minimized three-phase PWM boost rectifier with high performance [8], [9]. In [10], a four-switch-based three-phase (TPFS) inverter topology is proposed to replace the traditional TPSS inverter. In addition, the TPFS converter endows the TPSS converter with the power semiconductor devices' fault-tolerant ability. However, compared with the TPSS converter, the TPFS converters are believed to have some disadvantages, such as the halved voltage utilization factor, the imbalanced input ac currents, and the voltage deviation of the dc-link capacitors. Thus, substantial research efforts have been made to improve the performance of the TPFS converter.

Regarding the PWM modulation of a TPFS converter, substantial researches have been focused on the elimination of the imbalanced input ac currents [11]–[20]. For the method discussed in [12], four active vectors are used per switching period, which increases the switching losses. Considering the switching losses, the SVM approach utilizing three basic vectors per switching period is a promising option. Due the absence of the zero vectors in the TPFS rectifier, the equivalent zero vectors are realized by the combination of the two opposite active vectors whose volt–second integral is equal to zero. Considering the utilized equivalent zero vectors, the SVM methods for the TPFS rectifier can be classified into three categories: the equivalent zero vector by two large-amplitude opposite vectors (LVSVM) [13]–[15], the equivalent zero vector by two small-amplitude opposite vectors (SVSVM) [16]–[19], and the nearest three vectors SVM method (NTSVM) [20]. An overview of modulation techniques for the TPFS rectifier is presented in [21]. In [21], the performance comparison of the hysteresis band current control, sinusoidal PWM, and space vector modulation is discussed. The SVM approach discussed in [21] is developed with the assumption of the identical voltage across the two capacitors. The approaches discussed in [13]–[21] require sector identification and real-time calculation of the trigonometric function. It should be noted that the focus in [13]–[21] is to eliminate the imbalanced three-phase current introduced by the capacitor voltage oscillation. However, the influence and comparison of the three SVM approaches on the ac current ripple have not been addressed yet. The current ripple is important for a TPFS rectifier, which influences the noise and loss in the rectifier and the load. The optimized SVM approach should possess the advantage of producing the smallest current ripple.

To achieve the same performance as the conventional TPSS rectifier, the modeling, modulation, and control of the TPFS rectifier are indispensable. In [22], the state-space averaging technique is implemented in the modeling of the TPFS rectifier. However, the introduced model from which the closed-form control law is derived is a steady-state equation, and the dynamic response of the current of the TPFS rectifier is poor. The linearized dynamical models for the TPFS rectifier are developed in [23] and [24], and a hysteresis band is used to regulate the current. In [25], the direct power control is introduced as the

Manuscript received April 20, 2015; revised June 14, 2015 and July 29, 2015; accepted September 11, 2015. Date of publication September 22, 2015; date of current version January 28, 2016. This work was supported by the National Key Basic Research Program of China (973 Program) under Grant 2013CB035600. Recommended for publication by Associate Editor S. K. Panda.

The authors are with the College of Electrical Engineering, Zhejiang University, Hangzhou 310027, China (e-mail: zhyzeng@zju.edu.cn; weiyizheng@zju.edu.cn; rongxiang@zju.edu.cn; zhuchong@zju.edu.cn; yuanqingwei@zju.edu.cn).

Color versions of one or more of the figures in this paper are available online at http://ieeexplore.ieee.org.

Digital Object Identifier 10.1109/TPEL.2015.2480539

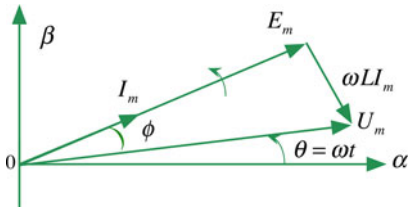

Fig. 1. Steady-state vector diagram of the PWM rectifier with a unity power factor.

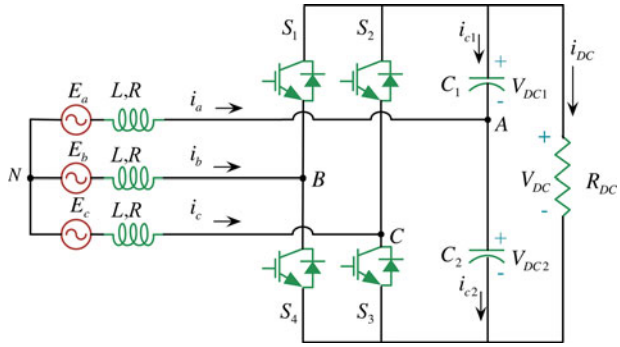

Fig. 2. Structure of a TPFS PWM boost rectifier.

control strategy for the TPFS rectifier. However, the hysteresis bands in [23]–[25] caused the harmonic current to be load dependent. Without any prespecified operating conditions, a model suitable for the controller design is developed in [26]. However, the proposed transfer function is developed with the assumption of identical voltages between the two capacitors. In [14], using double Fourier integral analysis, an accurate mathematical model is constructed to precisely describe the fundamental of the TPFS rectifier. However, the accurate mathematical model is not applicable to the design of system regulators because of its complexity. Compared with the conventional TPSS rectifier, a control-oriented small-signal model of the TPFS PWM rectifier is absent. A control-oriented small-signal model, accounting for the effect of capacitor voltage oscillation and deviation on the output voltage, is essential for the modulation and control of the TPFS rectifier. This paper is a continuation of the effort in [14], [22]–[26] to pursue a simple and accurate control-oriented model for the TPFSPWM rectifier aiming to achieve performance as excellent as that of the conventional TPSS rectifier.

A control-oriented model of the TPFS PWM rectifier is built in the *dq* synchronous frame, where the capacitor voltage oscillation and deviation have been taken into account. Three simple pulse width modulation methods using different combinations of the equivalent zero vector are developed, which can eliminate the ac component of the output voltage in the *dq* synchronous frame. To investigate the current performance of the three simple pulse width modulation methods, the current ripple root mean square (RMS), which is strongly related to the harmonic current [27]–[33], is selected as the criterion, and the analytical expressions in time domain are presented for assessment. Based on the analytical results, the method introducing the smallest ac current ripple is selected as the optimized SVM approach. The small-signal model for the TPFS rectifier is obtained by the linearization of the large-signal average models at the operating point, revealing a right-half plane (RHP) zero feature in the dc voltage control loop that is also existed in the TPSS rectifier. Therefore, a cascaded dual-loop control structure, widely adopted in the control of TPSS rectifiers, is used to control the TPFS PWM rectifier to alleviate the effect of the RHP zero on the system dynamics [34], [35]. For the purpose of eliminated capacitor voltage deviation and ac current improvement, a control strategy based on the *dq* synchronous frame is presented to realize real-time control of the capacitor voltage deviation.

Due to the capacitor voltage oscillation, the modulation index in [36] and [37] is not applicable to evaluate the modulation property of the TPFS rectifier. In this paper, a modulation evaluation function $f(V_{\rm DC}, I_m, \theta)$ is developed to evaluate the modulation property of the TPFS rectifier. It reveals that, with the improper combination of the ac current and the dc voltage, the TPFS rectifier operates alternately in the linear modulation region and the overmodulation region, generating the low-frequency harmonic current. Experimental results demonstrate that excellent current performance is achieved with comprehensive considerations of the modeling, modulation, and control strategy.

II. Low-Frequency Equivalent Modeling of the TPFS PWM Rectifier in the *dq* Synchronous Frame

The structure of a TPFS PWM boost rectifier is shown in Fig. 2. E_a, E_b, and E_c represent the grid voltages, and i_a, i_b, and i_c denote the input currents. Parameters *L* and *R* are the filter inductors and the parasitic resistance, respectively. $V_{\rm DC}$ represents the dc output voltage. C_1 and C_2 are the output capacitors, and the values of the two series-connected output capacitors are assumed to be identical ($C_1 = C_2$).

Fig. 1 shows the low-frequency steady-state vector diagram of the PWM rectifier with a unity power factor. In Fig. 1, *U* represents the voltage vector of the output mean voltage and *E* denotes the voltage vector of the grid voltage; *I* is the current vector of the three-phase input current (i_a, i_b, i_c); φ denotes the phase displacement of the voltage vector *E* and *U*, and ω is the fundamental frequency. According to Fig. 1, the following expressions are satisfied:

$$\begin{cases} U_m = \sqrt{E_m^2 + (\omega L I_m)^2} \\ \phi = \arctan\left(\dfrac{\omega L I_m}{E_m}\right) \\ i_a = I_m \cos(\theta + \phi) \end{cases} \tag{1}$$

where E_m denotes the amplitude of the grid voltage; I_m is the amplitude of the three-phase input current; U_m is the amplitude of the output voltage.

When obtaining the low-frequency model for the TPFS rectifier, the three-phase input currents (i_a, i_b, i_c), three-phase grid voltages (E_a, E_b, E_c) can be regarded as purely sinusoidal three-phase waveforms, whereas the actual output voltages of the TPFS rectifier are the high-frequency pulse waves. Thus, the mean value of the actual output voltage per switching period is used when obtaining the low-frequency equivalent modeling. By adopting the similar method presented in [35], the output

mean voltages of the rectifier with respect to *N* are expressed as

$$\begin{bmatrix} \overline{u_{AN}} \\ \overline{u_{BN}} \\ \overline{u_{CN}} \end{bmatrix} = \frac{1}{3}\begin{bmatrix} -1 & -1 \\ 2 & -1 \\ -1 & 2 \end{bmatrix}\begin{bmatrix} \overline{u_{BA}} \\ \overline{u_{CA}} \end{bmatrix} = \begin{bmatrix} \left(-\frac{1}{3}V_{\mathrm{DC2}} - \frac{1}{3}V_{\mathrm{DC1}}\right)d_b + \left(-\frac{1}{3}V_{\mathrm{DC2}} - \frac{1}{3}V_{\mathrm{DC1}}\right)d_c + \frac{1}{3}V_{\mathrm{DC2}} \\ \left(\frac{2}{3}V_{\mathrm{DC2}} + \frac{2}{3}V_{\mathrm{DC1}}\right)d_b + \left(-\frac{1}{3}V_{\mathrm{DC2}} - \frac{1}{3}V_{\mathrm{DC1}}\right)d_c - \frac{1}{3}V_{\mathrm{DC2}} \\ \left(-\frac{1}{3}V_{\mathrm{DC2}} - \frac{1}{3}V_{\mathrm{DC1}}\right)d_b + \left(\frac{2}{3}V_{\mathrm{DC2}} + \frac{2}{3}V_{\mathrm{DC1}}\right)d_c - \frac{1}{3}V_{\mathrm{DC2}} \end{bmatrix}. \tag{2}$$

Applying the Kirchhoff current law (KCL) to the dc side of the rectifier exhibited in Fig. 2, the expressions of the capacitor voltage dynamics are derived as

$$C\frac{dV_{\mathrm{DC2}}}{dt} = i_{c2} = -(1-d_b)i_b - (1-d_c)i_c - \frac{(V_{\mathrm{DC1}} + V_{\mathrm{DC2}})}{R_{\mathrm{DC}}} \tag{3}$$

$$C\frac{dV_{\mathrm{DC1}}}{dt} = i_{c1} = d_b i_b + d_c i_c - \frac{(V_{\mathrm{DC1}} + V_{\mathrm{DC2}})}{R_{\mathrm{DC}}}. \tag{4}$$

The dynamic equation of the dc-link voltage V_{DC} is obtained by adding (3) and (4)

$$C\frac{dV_{\mathrm{DC}}}{dt} = i_a + 2d_b i_b + 2d_c i_c - \frac{2V_{\mathrm{DC}}}{R_{\mathrm{DC}}}. \tag{5}$$

Applying the KCL to the split output capacitors in Fig. 2, the following expression is obtained:

$$C\frac{d(V_{\mathrm{DC2}} - V_{\mathrm{DC1}})}{dt} = -(i_c + i_b) = i_a. \tag{6}$$

Then, the analytical solution of (6) is deduced as

$$V_{\mathrm{DC2}}(t) - V_{\mathrm{DC1}}(t) = \int_0^t i_a dt + (V_{\mathrm{DC2}}(0) - V_{\mathrm{DC1}}(0)) \tag{7}$$

where $V_{\mathrm{DC2}}(0)$ is the initial voltage of C_2, and $V_{\mathrm{DC1}}(0)$ denotes the initial voltage of C_1.

Finally, the expressions of $V_{\mathrm{DC1}}(t)$ and $V_{\mathrm{DC2}}(t)$ are obtained, respectively, as

$$\begin{cases} V_{\mathrm{DC1}}(t) = \frac{1}{2}V_{\mathrm{DC}} - \frac{1}{2}\left(\int_0^t i_a dt + V_{\mathrm{DC2}}(0) - V_{\mathrm{DC1}}(0)\right) \\ V_{\mathrm{DC2}}(t) = \frac{1}{2}V_{\mathrm{DC}} + \frac{1}{2}\left(\int_0^t i_a dt + V_{\mathrm{DC2}}(0) - V_{\mathrm{DC1}}(0)\right). \end{cases} \tag{8}$$

Equation (8) reveals the effect of the current i_a on the capacitor voltage. The capacitor voltage oscillation is inherent in the TPFS rectifier. It should be noted that the dc component in (8) does not decay with time, which is the capacitor voltage deviation.

Considering Park's transformation, (5) is simplified as [35], [38]

$$C\frac{dV_{\mathrm{DC}}}{dt} = \frac{3}{2}i_q\left(-\frac{4}{3}d_b\sin\left(\omega t - \frac{2\pi}{3}\right) - \frac{4}{3}d_c\sin\left(\omega t + \frac{2\pi}{3}\right) - \frac{2}{3}\sin(\omega t)\right) + \frac{3}{2}i_d\left(\frac{4}{3}d_b\cos\left(\omega t - \frac{2\pi}{3}\right) + \frac{4}{3}d_c\cos\left(\omega t + \frac{2\pi}{3}\right) + \frac{2}{3}\cos(\omega t)\right) - \frac{2V_{\mathrm{DC}}}{R_{\mathrm{DC}}}. \tag{9}$$

Here, two equivalent duty ratios can be defined as

$$\begin{cases} d_d = \frac{4}{3}d_b\cos\left(\omega t - \frac{2\pi}{3}\right) + \frac{4}{3}d_c\cos\left(\omega t + \frac{2\pi}{3}\right) + \frac{2}{3}\cos(\omega t) \\ d_q = -\frac{4}{3}d_b\sin\left(\omega t - \frac{2\pi}{3}\right) - \frac{4}{3}d_c\sin\left(\omega t + \frac{2\pi}{3}\right) - \frac{2}{3}\sin(\omega t). \end{cases} \tag{10}$$

Then, the dynamic equation of the dc-link voltage V_{DC} can be further simplified as

$$C\frac{dV_{\mathrm{DC}}}{dt} = \frac{3}{2}(i_d d_d + i_q d_q) - \frac{2V_{\mathrm{DC}}}{R_{\mathrm{DC}}}. \tag{11}$$

Performing Park's transformation on (2) leads to

$$\begin{cases} \overline{u_{dN}} = \frac{2}{3}\cos\left(\omega t - \frac{2\pi}{3}\right)V_{\mathrm{DC}}d_b + \frac{2}{3}\cos\left(\omega t + \frac{2\pi}{3}\right)V_{\mathrm{DC}}d_c + \frac{2}{3}\cos(\omega t)V_{\mathrm{DC2}} \\ \overline{u_{qN}} = -\frac{2}{3}\sin\left(\omega t - \frac{2\pi}{3}\right)V_{\mathrm{DC}}d_b - \frac{2}{3}\sin\left(\omega t + \frac{2\pi}{3}\right)V_{\mathrm{DC}}d_c - \frac{2}{3}\sin(\omega t)V_{\mathrm{DC2}}. \end{cases} \tag{12}$$

Considering (10), (12) can be further simplified as

$$\begin{cases} \overline{u_{dN}} = \frac{1}{2}d_d V_{\mathrm{DC}} + \frac{1}{3}(V_{\mathrm{DC2}} - V_{\mathrm{DC1}})\cos(\omega t) \\ \overline{u_{qN}} = \frac{1}{2}d_q V_{\mathrm{DC}} - \frac{1}{3}(V_{\mathrm{DC2}} - V_{\mathrm{DC1}})\sin(\omega t). \end{cases} \tag{13}$$

Finally, performing Park's transformation on the model based on *abc* stationary frame developed by [22], [26] and considering (13) and (14), the low-frequency model in the *dq* synchronous frame is derived as

$$\begin{bmatrix} \frac{di_d}{dt} \\ \frac{di_q}{dt} \\ \frac{dV_{\mathrm{DC}}}{dt} \end{bmatrix} = \begin{bmatrix} \frac{-R}{L} & \omega L & 0 \\ -\omega L & \frac{-R}{L} & 0 \\ \frac{3}{2C}d_d & \frac{3}{2C}d_q & \frac{-2}{CR_{\mathrm{dc}}} \end{bmatrix}\begin{bmatrix} i_d \\ i_q \\ V_{\mathrm{DC}} \end{bmatrix} - \begin{bmatrix} \frac{\overline{u_{dN}}}{L} \\ \frac{\overline{u_{qN}}}{L} \\ 0 \end{bmatrix} + \begin{bmatrix} \frac{E_d}{L} \\ \frac{E_q}{L} \\ 0 \end{bmatrix}. \tag{14}$$

TABLE I
FOUR BASIC VECTORS IN THE $\alpha\beta$ STATIONARY FRAME FOR THE TPFS PWM RECTIFIER

S_b	S_c	Vector	u_α	u_β
0	0	V_{00}	$2V_{DC2}/3$	0
1	0	V_{10}	$(V_{DC2}-V_{DC1})/3$	$(V_{DC2}+V_{DC1})/\sqrt{3}$
1	1	V_{11}	$-2V_{DC1}/3$	0
0	1	V_{01}	$(V_{DC2}-V_{DC1})/3$	$-(V_{DC2}+V_{DC1})/\sqrt{3}$

where E_d and E_q represent the grid voltage component in the d-axis and q-axis, respectively.

With ignorance of the imbalanced voltage between the capacitor C_1 and C_2, the duty ratios for the d_b and d_c are [22], [26]

$$\begin{cases} d_b = \dfrac{1}{2} - \dfrac{3}{2}\dfrac{U_m}{V_{DC}}\cos(\omega t-\phi) + \dfrac{\sqrt{3}}{2}\dfrac{U_m}{V_{DC}}\sin(\omega t-\phi) \\ d_c = \dfrac{1}{2} - \dfrac{3}{2}\dfrac{U_m}{V_{DC}}\cos(\omega t-\phi) - \dfrac{\sqrt{3}}{2}\dfrac{U_m}{V_{DC}}\sin(\omega t-\phi). \end{cases} \tag{15}$$

Substituting (10) and (15) into (12), the voltage components in the d-axis and q-axis of the low-frequency output voltage are

$$\begin{cases} \overline{u_{dN}} = U_m\cos(\phi) + \dfrac{1}{3}(V_{DC2}-V_{DC1})\cos(\omega t) \\ \overline{u_{qN}} = U_m\sin(\phi) - \dfrac{1}{3}(V_{DC2}-V_{DC1})\cos(\omega t). \end{cases} \tag{16}$$

Equation (16) indicates that the imbalanced voltage between the capacitor C_1 and C_2 ($V_{DC1} \neq V_{DC2}$) introduces the ac voltage component to the output voltage of the rectifier in the dq synchronous frame, which seriously deteriorates the quality of the input current.

III. SIMPLE SPACE VECTOR MODULATION METHOD FOR THE TPFS PWM RECTIFIER

The vectors of the TPFS rectifier are given in Table I [13]. Compared with the TPSS rectifier, only four voltage vectors are available, and the zero vectors are absent in the TPFS rectifier. Considering the low frequency, the steady-state vector diagram shown in Fig. 1, the following assumptions are made to develop the SVM approach:

$$\begin{cases} \overline{u_{AN}} = u^*_{AN} = U_m\cos(\theta) \\ \overline{u_{BN}} = u^*_{BN} = U_m\cos(\theta-2\pi/3) \\ \overline{u_{CN}} = u^*_{CN} = U_m\cos(\theta+2\pi/3) \end{cases} \tag{17}$$

where u^*_{AN}, u^*_{BN} and u^*_{CN} denote the reference output voltage and θ is the voltage vector position.

For the TPFS rectifier, two combinations for the equivalent zero vector are available, as shown in Fig. 3, V_{11}-V_{00} and V_{01}-V_{10}. For the LVSVM, three vectors (V_{01}, V_{10}, V_{00}) are used in sectors I and IV; three vectors (V_{01}, V_{10}, V_{11}) are adopted in sectors II and III, as shown in Fig. 3(a). While for the SVSVM, three vectors (V_{11}, V_{10}, V_{00}) are applied in sectors I and IV; three vectors (V_{11}, V_{01}, V_{00}) are used in sectors II and III. The

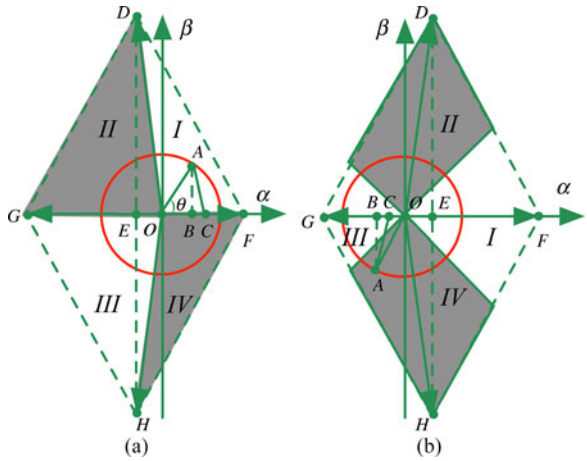

Fig. 3. Vectors in the $\alpha\beta$ plane for the TPFS rectifier. (a) SVSVM and LVSVM. (b) NTSVM.

vector plane of the TPFS rectifier using the NTSVM is shown in Fig. 3(b). For the NTSVM, three vectors (V_{01}, V_{10}, V_{00}) are applied in sector I; three vectors (V_{00}, V_{11}, V_{10}) are applied in sector II; the vectors V_{10}, V_{11} and V_{01} are implemented in sector III; three vectors (V_{01}, V_{11}, V_{00}) are used in sector IV.

In Fig. 3, line segments $|OF|$, $|OG|$, $|OD|$, and $|OH|$ denote the vector V_{00}, V_{11}, V_{10}, and V_{01}, respectively. The line segment $|DE|$ is the β-axis component of the vector V_{10}, the line segment $|OE|$ represents the α-axis component of the vector V_{10}. The line segment $|OA|$ denotes the reference U_r, and line segments $|AB|$ and $|OB|$ represent the β-axis component $U_{r\beta}$ and the α-axis component $U_{r\alpha}$ of the reference U_r, respectively. According to Fig. 3, the following expressions are satisfied:

$$\begin{cases} |OB| = u^*_{AN} \\ |AB| = \dfrac{u^*_{BN}-u^*_{CN}}{\sqrt{3}} \end{cases}. \tag{18}$$

In SVSVM, a case study for sectors I and II is performed, where the reference vector U_r is decomposed into $U_{r\alpha}$ and $U_{r\beta}$ in the $\alpha\beta$ stationary frame

$$\begin{cases} d_{00}\,|OF| + d_{10}\,|OE| + d_{11}\,|OG| = |OB| \\ d_{10}\,|DE| = |AB| \\ d_{10} + d_{00} + d_{11} = 1 \end{cases} \tag{19}$$

where d_{10}, d_{00}, and d_{11} denote the duty ratios of the vectors V_{10}, V_{00}, and V_{11}, respectively.

The solutions of (19) are

$$\begin{cases} d_{11} = \dfrac{V_{DC2}+u^*_{CN}-u^*_{AN}}{V_{DC1}+V_{DC2}} \\ d_{00} = \dfrac{V_{DC1}+u^*_{AN}-u^*_{BN}}{V_{DC1}+V_{DC2}} \\ d_{10} = \dfrac{u^*_{BN}-u^*_{CN}}{V_{DC1}+V_{DC2}}. \end{cases} \tag{20}$$

Using a similar approach, the duty ratios for the three active vectors (V_{11}, V_{00}, V_{01}) in sectors III and IV are derived and shown in Table II.

TABLE II
ALLOCATED DUTY RATIOS OF THE SVSVM STRATEGY

Sector	d_{11}	d_{01}	d_{10}	d_{00}
I, II	$\frac{V_{\mathrm{DC}2}+u^*_{CN}-u^*_{AN}}{V_{\mathrm{DC}1}+V_{\mathrm{DC}2}}$	0	$\frac{u^*_{BN}-u^*_{CN}}{V_{\mathrm{DC}1}+V_{\mathrm{DC}2}}$	$\frac{V_{\mathrm{DC}1}+u^*_{AN}-u^*_{BN}}{V_{\mathrm{DC}1}+V_{\mathrm{DC}2}}$
III, IV	$\frac{V_{\mathrm{DC}2}+u^*_{BN}-u^*_{AN}}{V_{\mathrm{DC}1}+V_{\mathrm{DC}2}}$	$\frac{u^*_{CN}-u^*_{BN}}{V_{\mathrm{DC}1}+V_{\mathrm{DC}2}}$	0	$\frac{V_{\mathrm{DC}1}+u^*_{AN}-u^*_{CN}}{V_{\mathrm{DC}1}+V_{\mathrm{DC}2}}$

Similarly, for the LVSVM strategy, the duty ratios for the three active vectors are listed in Table III.

For the NTSVM strategy, when the reference vector U_r is located in sector I, the duty ratios for three vectors are identical with that of the LVSVM in sector I, as listed in Table III; the duty ratios of the NTSVM in sector II are the same as that of the SVSVM in sector I; the duty ratios of the NTSVM in sector III are consistent with that of the LVSVM in sector II; the duty ratios of the NTSVM in sector IV are identical with that of SVSVM in sector II, as listed in Table II.

Taking into account that the symmetrical placement of pulses produces fewer harmonics, the time sequence with the symmetrical characteristic is selected as the scalar of the PWM, as shown in Figs. 4 and 5.

As shown in Fig. 5, for the SVSVM modulation strategy, the duty ratios d_b and d_c in sectors I and II are

$$\begin{cases} d_b = d_{11} + d_{10} = \dfrac{V_{\mathrm{DC}2} - u^*_{AN} + u^*_{BN}}{V_{\mathrm{DC}1} + V_{\mathrm{DC}2}} \\ d_c = d_{11} = \dfrac{V_{\mathrm{DC}2} - u^*_{AN} + u^*_{CN}}{V_{\mathrm{DC}1} + V_{\mathrm{DC}2}}. \end{cases} \tag{21}$$

For the SVSVM modulation strategy, the duty ratios d_{b} and d_{c} in sectors III and IV are

$$\begin{cases} d_b = d_{11} = \dfrac{V_{\mathrm{DC}2} - u^*_{AN} + u^*_{BN}}{V_{\mathrm{DC}1} + V_{\mathrm{DC}2}} \\ d_c = d_{01} + d_{11} = \dfrac{V_{\mathrm{DC}2} - u^*_{AN} + u^*_{CN}}{V_{\mathrm{DC}1} + V_{\mathrm{DC}2}}. \end{cases} \tag{22}$$

Equations (21) and (22) are identical to each other, which indicates that, in the entire vector plane, the SVSVM approaches have a unified algorithm expression. Using the similar method, the duty ratios d_b and d_c of the LVSVM and the NTSVM in the entire vector plane are obtained, which are consistent with (21) and (22). Therefore, in the entire vector plane, the SVSVM, LVSVM, and NTSVM approaches have a unified algorithm expression, where the sector identification and the real-time calculation of the trigonometric function are not required. Additionally, the proposed modulation approach provides sufficient insight on how to implement the pulse width modulation in the software.

IV. EFFECT OF THE MODULATION STRATEGY ON THE CURRENT RIPPLE

In this section, the analysis of current ripple is performed per switching period. The low-frequency model is not available for the current ripple analysis. The actual currents should include high-frequency current ripple i_{rip}. Thus, the high-frequency model for the TPFS rectifier is [39]

$$\begin{cases} E_a = L\dfrac{d\left(i_a + i_{\mathrm{rip}a}\right)}{dt} + R\left(i_a + i_{\mathrm{rip}a}\right) + u_{AN} \\ E_b = L\dfrac{d\left(i_b + i_{\mathrm{rip}b}\right)}{dt} + R\left(i_b + i_{\mathrm{rip}b}\right) + u_{BN} \\ E_c = L\dfrac{d\left(i_c + i_{\mathrm{rip}c}\right)}{dt} + R\left(i_c + i_{\mathrm{rip}c}\right) + u_{CN} \end{cases} \tag{23}$$

where the $i_{\mathrm{rip}a}$, $i_{\mathrm{rip}b}$, and $i_{\mathrm{rip}c}$ denote current ripple included in the actual three-phase input current.

The low-frequency model is

$$\begin{cases} E_a = L\dfrac{di_a}{dt} + Ri_a + \overline{u_{AN}} \\ E_b = L\dfrac{di_b}{dt} + Ri_b + \overline{u_{BN}} \\ E_c = L\dfrac{di_c}{dt} + Ri_c + \overline{u_{CN}}. \end{cases} \tag{24}$$

Subtracting (24) from (23) and considering (17) leads to

$$\begin{cases} 0 = L\dfrac{di_{\mathrm{rip}a}}{dt} + Ri_{\mathrm{rip}a} + \left(u_{AN} - u^*_{AN}\right) \\ 0 = L\dfrac{di_{\mathrm{rip}b}}{dt} + Ri_{\mathrm{rip}b} + \left(u_{BN} - u^*_{BN}\right) \\ 0 = L\dfrac{di_{\mathrm{rip}c}}{dt} + Ri_{\mathrm{rip}c} + \left(u_{CN} - u^*_{CN}\right). \end{cases} \tag{25}$$

Then, ignoring the parasitic resistance *R*, the expression for the current ripple is further simplified as [39]

$$\begin{cases} i_{\mathrm{rip}a} = \dfrac{\left(u_{AN} - u^*_{AN}\right)}{L} T_s \\ i_{\mathrm{rip}b} = \dfrac{\left(u_{BN} - u^*_{BN}\right)}{L} T_s \\ i_{\mathrm{rip}c} = \dfrac{\left(u_{CN} - u^*_{CN}\right)}{L} T_s. \end{cases} \tag{26}$$

The total current ripple of the TPFS rectifier is defined as

$$i_{\mathrm{rip}} = \sqrt{i^2_{\mathrm{rip}a} + i^2_{\mathrm{rip}b} + i^2_{\mathrm{rip}c}} = \sqrt{\frac{3}{2}\left(i^2_{\mathrm{rip}\alpha} + i^2_{\mathrm{rip}\beta}\right)} \tag{27}$$

where $i_{\mathrm{rip}\alpha}$ denotes the current ripple in the α-axis and $i_{\mathrm{rip}\beta}$ is the current ripple in the β-axis. It should be noted that the mean value of the current ripple $(i_{\mathrm{rip}\alpha}, i_{\mathrm{rip}\beta})$ is zero in each switching period T_s. As shown in Figs. 4 and 5, the placement of the basic vector is symmetrical. Thus, instead of calculating the RMS value over the entire switching period, the RMS value analysis of the current ripple can be focused on the first half of the switching period

$$\begin{aligned} I_{\mathrm{ripRMS}} &= \sqrt{\frac{2}{T_s}\int_0^{\frac{T_s}{2}} i^2_{\mathrm{rip}} dt} \\ &= \sqrt{\frac{2}{T_s}\int_0^{\frac{T_s}{2}} \frac{3}{2}\left(i^2_{\mathrm{rip}\alpha} + i^2_{\mathrm{rip}\beta}\right) dt}. \end{aligned} \tag{28}$$

TABLE III
ALLOCATED DUTY RATIOS OF THE LVSVM STRATEGY

Sector	d_{11}	d_{01}	d_{10}	d_{00}
I, IV	0	$\frac{V_{DC2}+u^*_{CN}-u^*_{AN}}{V_{DC1}+V_{DC2}}$	$\frac{V_{DC2}+u^*_{BN}-u^*_{AN}}{V_{DC1}+V_{DC2}}$	$\frac{V_{DC1}-V_{DC2}+3u^*_{AN}}{V_{DC1}+V_{DC2}}$
II, III	$\frac{V_{DC2}-V_{DC1}-3u^*_{AN}}{V_{DC1}+V_{DC2}}$	$\frac{V_{DC1}+u^*_{AN}-u^*_{BN}}{V_{DC1}+V_{DC2}}$	$\frac{V_{DC1}+u^*_{AN}-u^*_{CN}}{V_{DC1}+V_{DC2}}$	0

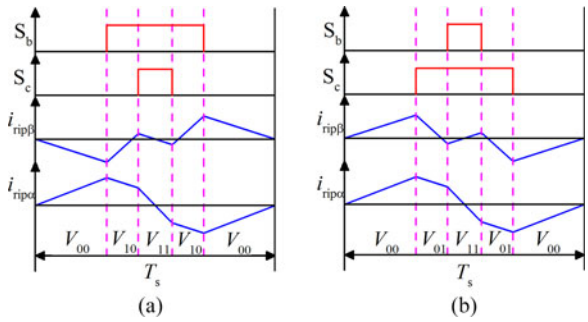

Fig. 4. Timing of space vectors and the current ripple. (a) Sectors I and II for the SVSVM, sector II for the NTSVM. (b) Sectors III and IV for the SVSVM, sector IV for the NTSVM.

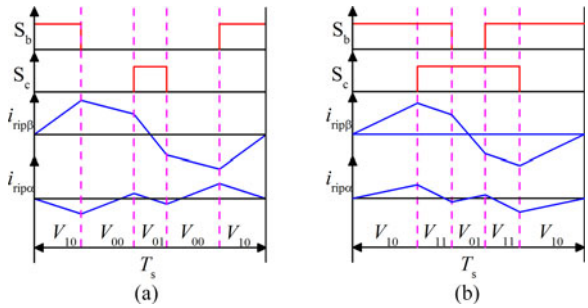

Fig. 5. Timing of space vectors and the current ripple. (a) Sectors I and IV for the LVSVM, sector I for the NTSVM. (b) Sectors II and III for the LVSVM, sector III for the NTSVM.

A case study is performed in sectors I and II. For the SVSVM modulation approach, the T_1 and T_2 are defined as

$$\begin{cases} T_1 = d_{00}T_s \\ T_2 = d_{10}T_s \end{cases}. \tag{29}$$

The expression for the current ripples $i_{\mathrm{rip}\alpha}$ and $i_{\mathrm{rip}\beta}$ are derived with the assumption of $V_{\mathrm{DC1}} = V_{\mathrm{DC2}} = V_{\mathrm{DC}}/2$

$$i_{r\alpha} = \begin{cases} \dfrac{u_{\mathrm{rip}\alpha 1}}{L}t, & 0 < t < \dfrac{T_1}{2} \\ \dfrac{u_{\mathrm{rip}\alpha 2}}{L}\left(t - \dfrac{T_1}{2}\right) + \dfrac{u_{\mathrm{rip}\alpha 1}T_1}{2L}, & \dfrac{T_1}{2} < t < \dfrac{T_1+T_2}{2} \\ \dfrac{u_{\mathrm{rip}\alpha 3}}{L}\left(t - \dfrac{T_s}{2}\right), & \dfrac{T_1+T_2}{2} < t < \dfrac{T_s}{2} \end{cases} \tag{30}$$

$$i_{r\beta} = \begin{cases} \dfrac{u_{\mathrm{rip}\beta 1}}{L}t, & 0 < t < \dfrac{T_1}{2} \\ \dfrac{u_{\mathrm{rip}\beta 2}}{L}\left(t - \dfrac{T_1}{2}\right) + \dfrac{u_{\mathrm{rip}\beta 1}T_1}{2L}, & \dfrac{T_1}{2} < t < \dfrac{T_1+T_2}{2} \\ \dfrac{u_{\mathrm{rip}\beta 3}}{L}\left(t - \dfrac{T_s}{2}\right), & \dfrac{T_1+T_2}{2} < t < \dfrac{T_s}{2} \end{cases} \tag{31}$$

where

$$\begin{cases} u_{\mathrm{rip}\alpha 1} = \dfrac{V_{\mathrm{DC}}}{3} - u^*_{\alpha N} \\ u_{\mathrm{rip}\alpha 2} = -u^*_{\alpha N} \\ u_{\mathrm{rip}\alpha 3} = -\dfrac{V_{\mathrm{DC}}}{3} - u^*_{\alpha N} \end{cases} \tag{32}$$

$$\begin{cases} u_{\mathrm{rip}\beta 1} = -u^*_{\beta N} \\ u_{\mathrm{rip}\beta 2} = \dfrac{V_{\mathrm{DC}}}{\sqrt{3}} - u^*_{\beta N} \\ u_{\mathrm{rip}\beta 1} = -u^*_{\beta N} \end{cases} \tag{33}$$

$$\begin{cases} u^*_{\alpha N} = U_m\cos(\theta) \\ u^*_{\beta N} = U_m\sin(\theta) \end{cases}. \tag{34}$$

Substituting (29)–(34) into (28) and accounting for Fig. 4, the RMS value of the current ripple for the SVSVM strategy is

$$\begin{aligned} I_{\mathrm{ripRMS}} = \frac{T_s}{24LV_{\mathrm{DC}}}(&54U_m^4 - 423U_m^4\cos^4\theta \\ &+ 540U_m^4\cos^2\theta - 24\sqrt{3}U_m^3V_{\mathrm{DC}}\left|\sin^3\theta\right| \\ &- 36U_m^2V_{\mathrm{DC}}^2\cos^2\theta + 2V_{\mathrm{DC}}^4)^{1/2}. \end{aligned} \tag{35}$$

Similarly, the RMS value of the current ripple for the LVSVM strategy is obtained as

$$\begin{aligned} I_{\mathrm{ripRMS}} = \frac{T_s}{24LV_{\mathrm{DC}}}(&54U_m^4 - 423U_m^4\cos^4\theta + 540U_m^4\cos^2\theta \\ &+ 216U_m^3V_{\mathrm{DC}}\left|\cos^3\theta\right| - 36U_m^2V_{\mathrm{DC}}^2 \\ &- 108U_m^2V_{\mathrm{DC}}^2\cos^2\theta + 6V_{\mathrm{DC}}^4)^{1/2}. \end{aligned} \tag{36}$$

For the NTSVM modulation strategy, the expressions of the current ripple RMS in sectors I and III are identical with (36), and the expressions of the current ripple RMS in sectors II and IV are identical with (35).

In addition to the circuit parameters listed in Table IV, the RMS value of the current ripple highly depends on the dc voltage and the vector angle of the reference voltage. The circuit

TABLE IV
SYSTEM PARAMETERS

R_s	L	U_m	ω
0.1 Ω	3 mH	160 V	314 rad/s
E_a / E_b / E_c	I_m	P	C
110 V	25 A	6 kW	2200 μF
Sampling rate of the closed-loop system	Discretization method	Switching frequency	Switching period T_s
10 kHz	Zero-order hold	10 kHz	0.0001s

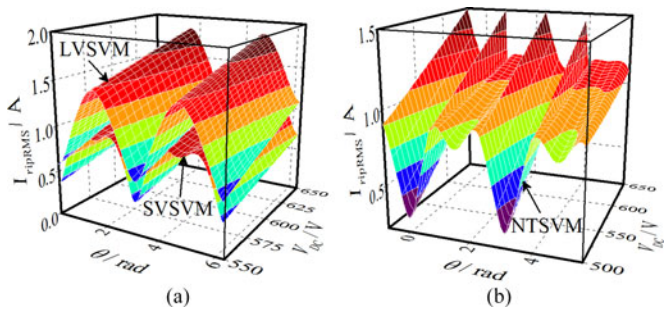

Fig. 6. RMS value of the current ripple versus the dc voltage $V_{\rm DC}$ and the vector phase angle θ. (a) SVSVM and LVSVM. (b) NTSVM.

parameters listed in Table IV are substituted into (35), (36), and the RMS values of the current ripple using SVSVM, LVSVM, and NTSVM are analyzed and exhibited in Fig. 6, where the dc voltage ranges from 550 to 650 V; in addition, the vector angle θ ranges from 0 to 2π. Fig. 6(a) shows that, regardless of the dc voltage and the vector angle of the reference voltage, the RMS value of the current ripple of LVSVM is higher than that of the SVSVM modulation scheme. It can be concluded from Fig. 6(b) that the RMS value of the current ripple of SVSVM is identical with that of NTSVM in the sectors II or sector IV; the RMS value of the current ripple of NTSVM is identical with that of LVSVM in the sectors I or sector III.

Considering the current performance, SVSVM is superior to the LVSVM and NTSVM modulation methods. Thus, with the purpose of the current ripple reduction, the SVSVM modulation strategy is adopted as the optimal modulation technique. It is worth noting that the RMS values of the current ripple increase with the increasing dc voltage.

V. CONTROL OF THE TPFS PWM RECTIFIER IN THE *dq* SYNCHRONOUS FRAME

As analyzed above, the model of the TPFS rectifier highly depends on the modulation strategy; an improper modulation strategy introduces an ac component into the output voltage of the TPFS rectifier, altering the model of the TPFS rectifier.

Substituting (21) into (12) leads to

$$\begin{cases} \overline{u_{dN}} = \frac{1}{2} d_d V_{\rm DC} = U_m \cos(\phi) \\ \overline{u_{qN}} = \frac{1}{2} d_q V_{\rm DC} = U_m \sin(\phi) \end{cases}. \tag{37}$$

Equation (37) indicates that the grid-frequency-related ac voltage component, introduced by the capacitor voltage oscillation ($V_{\rm DC1} \neq V_{\rm DC2}$), is eliminated by the proposed SVM method. Thus, with the grid-voltage orientation control ($E_q = 0$) and the feedforward decoupling, the low-frequency equivalent model for the TPFS rectifier becomes [35], [38]

$$\begin{cases} L\dfrac{di_d}{dt} + Ri_d = E_d - \dfrac{1}{2} d_d V_{\rm DC} \\ L\dfrac{di_q}{dt} + Ri_q = -\dfrac{1}{2} d_q V_{\rm DC} \\ C\dfrac{dV_{\rm DC}}{dt} = \dfrac{3}{2}(d_d i_d + d_q i_q) - \dfrac{2V_{\rm DC}}{R_{\rm DC}}. \end{cases} \tag{38}$$

It should be noted that, with the proposed SVM method, the model of the TPFS PWM rectifier is similar to that of the TPSS PWM rectifier proposed by [35], [38]. Thus, the model for the TPFS rectifier is decoupled into two SISO systems in which the *q*-axis system determines the power factor and the *d*-axis system regulates the power delivery [35], [38].

TABLE V
PARAMETERS OF THE PI CONTROLLERS

	d-axis current loop	*q*-axis current loop	Outer DC voltage loop	Capacitor voltage deviation control
K_p	15	15	0.5	0.08
K_I	1500	1500	130	0

A. PI Controller for the Current Loop

The small-signal transfer function can be established by ignoring the high-frequency disturbances. From (37), the operating point for d_d and d_q can be express as

$$\begin{cases} D_d = 2U_m \cos(\phi)/V_{\rm DC} \\ D_q = 2U_m \sin(\phi)/V_{\rm DC}. \end{cases} \tag{39}$$

Also, the operating point for i_d and $V_{\rm DC}$ be solved from (38)

$$\begin{cases} I_d = \dfrac{8E_d}{3D_d^2 R_{\rm DC}} \\ V_{\rm DC} = \dfrac{2E_d}{D_d}. \end{cases} \tag{40}$$

With the method proposed by [35], [38], the small-signal transfer functions from the duty ratio to the current are

$$\frac{i_d(s)}{d_d(s)} = \frac{32E_d}{R_{\rm DC}(1-D_d)^3} \frac{(1+R_{\rm DC}Cs/4)}{\left(1+\frac{16Ls}{3R_{\rm DC}(1-D_d)^2}+\frac{8LCs^2}{3(1-D_d)^2}\right)} \tag{41}$$

$$\frac{i_q(s)}{d_q(s)} = \frac{V_{\rm DC}/R}{(L/R)s+1} \tag{42}$$

where $i_d(s)$ is the Laplace transform of $i_d(t)$; $d_d(s)$ is the Laplace transform of $d_d(t)$; $i_q(s)$ is the Laplace transform of $i_q(t)$; $d_q(s)$ is the Laplace transform of $d_d(t)$.

The circuit parameters listed in Table V are substituted into (41) and (42), and the controllers are tuned by the conventional

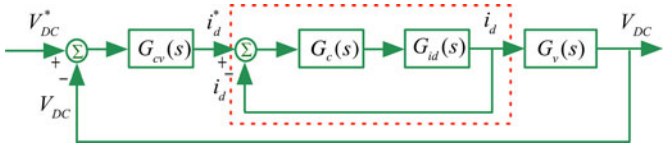

Fig. 7. Structures of the dual-loop control scheme for the TPFS PWM rectifier.

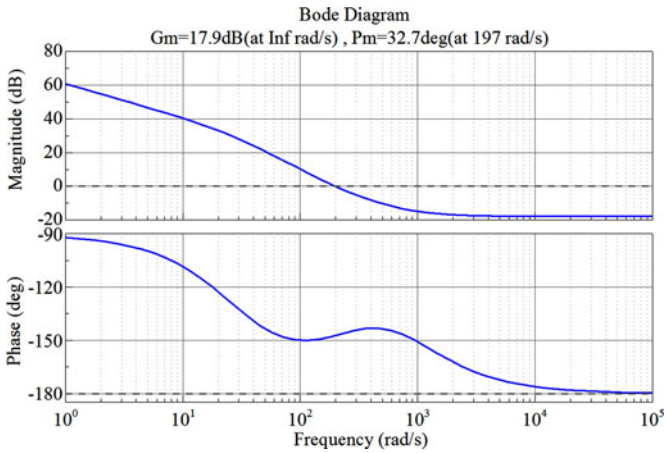

Fig. 8. Bode diagram of the dc voltage loop.

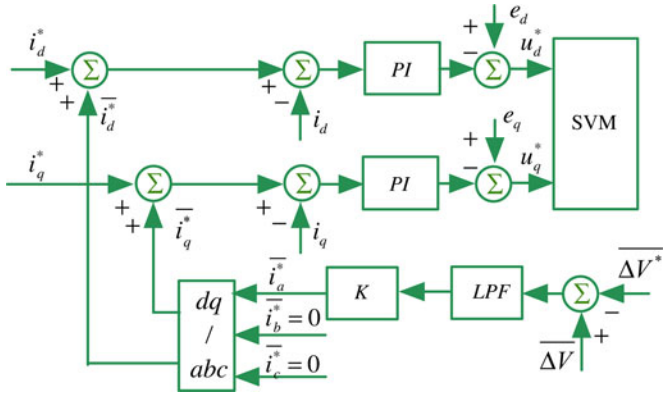

Fig. 9. block diagram of the control strategy for the deviation of the capacitor voltage.

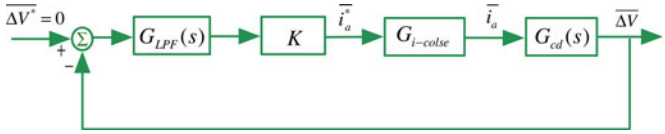

Fig. 10. Control structures of the deviation of the capacitor voltage for the TPFT PWM rectifier.

method [35], [38]. The parameters of the PI controller are listed in Table V.

B. PI Controller for the Voltage Loop

With the method proposed by [35], [38], the small-signal transfer functions from the *d*-axis current to the dc voltage are

$$G_V(s) = \frac{V_{\rm DC}(s)}{i_d(s)} = \frac{3R_{\rm DC}(1-D_d)}{16}\frac{\left(1-\frac{16}{3}\frac{Ls}{R_{\rm DC}(1-D_d)^2}\right)}{(1+R_{\rm DC}Cs/4)}. \tag{43}$$

In Fig. 7, $G_{cv}(s)$ denotes the transfer function of the voltage controller, and $G_{id}(s)$ is the transfer function of the d-axis current loop and $G_c(s)$ denotes the transfer function of the d-axis current controller. It is worth noting that the transfer function $G_V(s)$ contains a RHP zero. For the design of a dc voltage loop, the first thing is to investigate the location of the RHP zero and to alleviate the effect of the RHP zero on the system dynamics. By substituting the parameters in Table IV into (43), the PI controller for the dc voltage loop is tuned by the conventional method [35], [40] and the Bode diagram is exhibited in Fig. 8, where the crossover frequency (190 rad/s) is 1/6th of the corner frequency (1100 rad/s) of the RHP zero.

C. Control of the Capacitor Voltage Deviation

The dynamic equation for the capacitor voltage deviation is shown as

$$C\frac{d(V_{\rm DC2}-V_{\rm DC1})}{dt} = -(i_c+i_b) = i_a. \tag{44}$$

After the transient state, transient dc current $\overline{i}_a$ is introduced into the current i_a. Then, the analytical solution of (44) is

$$V_{\rm DC2}(t) - V_{\rm DC1}(t) = \frac{1}{C}\int i_a dt + \frac{1}{C}\int \overline{i}_a dt + (V_{\rm DC2}(0) - V_{\rm DC1}(0)). \tag{45}$$

Equation (45) reveals that, when the capacitor voltage deviation occurs, adding a proper dc component into current i_a can eliminate the capacitor voltage deviation. The transfer function can, therefore, be expressed as

$$G_{cd}(s) = \frac{\overline{V}(s)}{\overline{i}_a(s)} = \frac{1}{Cs}. \tag{46}$$

The block diagram of the control strategy for the deviation of the capacitor voltage is shown in Fig. 9. The voltage difference between C_1 and C_2 is measured in real time, and the deviation of the capacitor voltage is extracted from the voltage difference using the low-pass filter (LPF). Once the capacitor voltage deviation occurs, the feedforward path is activated to add the corresponding $\overline{i}_a$ into the reference current to eliminate the capacitor voltage deviation. Due to the implementation of the proportional controller, the feedforward path shown in Fig. 9 disconnects from the current loop when the capacitor voltage deviation is eliminated and does not affect the control of the TPFS PWM rectifier in normal operation.

With consideration of (44)–(46), the control structures of the deviation of the capacitor voltage for the TPFS PWM rectifier are shown in Fig. 10, where $G_{\rm LPF}(s)$ is the transfer function of a second-order LPF. According to Fig. 10, the open-loop transfer function of the voltage variation control loop can be expressed

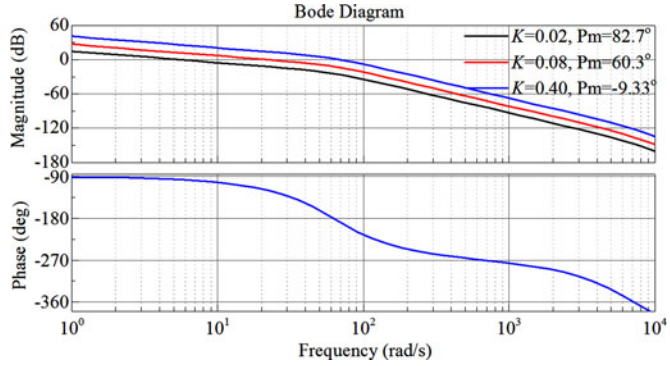

Fig. 11. Block diagram of the control strategy for the deviation of the capacitor voltage.

TABLE VI
DUTY RATIOS OF THE EQUIVALENT ZERO VECTORS

Sector	I	II
$d_{\rm zero}$	$\frac{V_{\rm DC2}-u^*_{AN}+u^*_{CN}}{V_{\rm DC}}$	$\frac{V_{\rm DC1}+u^*_{AN}-u^*_{BN}}{V_{\rm DC}}$
Sector	III	IV
$d_{\rm zero}$	$\frac{V_{\rm DC1}+u^*_{AN}-u^*_{CN}}{V_{\rm DC}}$	$\frac{V_{\rm DC2}-u^*_{AN}-u^*_{BN}}{V_{\rm DC}}$

as

$$G_{\rm offset}(s) = \frac{\overline{\Delta V}(s)}{\overline{i_a}(s)} = G_{\rm LPF}(s)\cdot K\cdot G_{i-{\rm close}}(s)\cdot G_{cd}(s) \quad (47)$$

$$G_{i-{\rm close}}(s) \approx 1. \quad (48)$$

$G_{i-{\rm close}}(s)$ is the closed-loop transfer function of current control loop, and can be approximated as 1 due to its high bandwidth compared with the voltage variation control loop [2].

In Fig. 10, parameter *K* denotes a proportional controller. The controller designed is based on the transfer function $G_{\rm offset}(s)$, and the Bode diagram of the open-loop transfer function is drawn in Fig. 11. Due to the already existing integral item in $G_{\rm offset}(s)$, zero steady error is achieved with a simple proportional controller. In Fig. 11, *K* is set to be 0.02, 0.08, and 0.4, respectively. It can be concluded from Fig. 11 that a larger *K* improves the bandwidth of the system, and, thus, a better dynamic performance is achieved. However, the stability of the system deteriorates with increasing *K*. Hence, *K* is set to 0.08, which obtains a performance that is a compromise between dynamics and stability.

VI. NOVEL LINEAR MODULATION INDEX FUNCTION FOR THE TPFS PWM RECTIFIER

The duty ratio of the equivalent zero vector is used to evaluate the property of the modulation of the TPFS PWM rectifier. The negative value of the duty ratio, allocated for the equivalent zero vectors, indicates the overmodulation state. According to Table II, the duty ratios of the equivalent zero vectors are listed in Table VI. It should be noted that the low-frequency model is used for the analysis of the modulation property. Considering the symmetry of the input voltage, the analysis of modulation is focused on the sectors I and II.

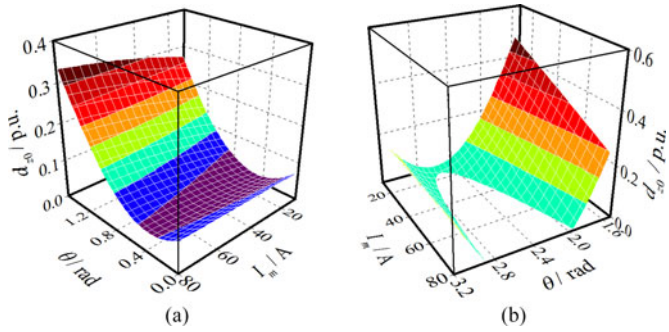

Fig. 12. Value of the modulation performance evaluation function ($V_{\rm DC}$ = 560 V) versus the amplitude and the vector angle of the converter output voltage. (a) First quadrant. (b) Second quadrant.

Considering (1), (45) is rewritten as

$$\begin{cases} V_{\rm DC1}(t) = \frac{1}{2}V_{\rm DC} - \frac{1}{2}\frac{I_m\sin(\phi+\theta)}{\omega C} - \frac{\overline{\Delta V}}{2} \\ V_{\rm DC2}(t) = \frac{1}{2}V_{\rm DC} + \frac{1}{2}\frac{I_m\sin(\phi+\theta)}{\omega C} + \frac{\overline{\Delta V}}{2}. \end{cases} \quad (49)$$

According to Table VI, the conditions for the linear modulation are

$$\begin{cases} \frac{V_{\rm DC2}}{V_{\rm DC}} \geq \frac{u^*_{CN}-u^*_{AN}}{V_{\rm DC}}, & {\rm sector I} \\ \frac{V_{\rm DC1}}{V_{\rm DC}} \geq \frac{u^*_{AN}-u^*_{BN}}{V_{\rm DC}}, & {\rm sector II}. \end{cases} \quad (50)$$

Considering (1), (49), and (50), a modulation performance evaluation function is defined as

$$f(V_{\rm DC}, I_m, \theta) = \begin{cases} -\frac{1}{V_{\rm DC}}\sqrt{3\left(E_m^2+(\omega L I_m)^2\right)}\sin\left(\theta+\frac{\pi}{3}\right) \\ \quad +\frac{1}{2}+\frac{I_m\sin(\theta+\phi)}{2\omega V_{\rm DC}C}+\frac{\overline{\Delta V}}{2V_{\rm DC}}, & {\rm sector\ I} \\ -\frac{1}{V_{\rm DC}}\sqrt{3\left(E_m^2+(\omega L I_m)^2\right)}\sin\left(\theta-\frac{\pi}{3}\right) \\ \quad +\frac{1}{2}-\frac{I_m\sin(\theta+\phi)}{2\omega V_{\rm DC}C}-\frac{\overline{\Delta V}}{2V_{\rm DC}}, & {\rm sector\ II} \end{cases} . \quad (51)$$

Once the capacitor voltage deviation is eliminated by the proposed method ($\Delta V = 0$), the amplitude of ac input current, the dc voltage, and the reference voltage vector angle determine the value of the modulation performance evaluation function. When the value of function $f(V_{\rm DC}, I_m, \theta)$ is less than zero, the duty ratio allocated for the equivalent zero vector becomes negative, which indicates overmodulation. The circuit parameters listed in Table IV are substituted into (51), and analytical results are shown in Fig. 12, where the amplitude of the ac input current I_m ranges from 10 to 80 A and the vector angle θ ranges from 0 to 2π. Additionally, the analytical results exhibited in Fig. 12

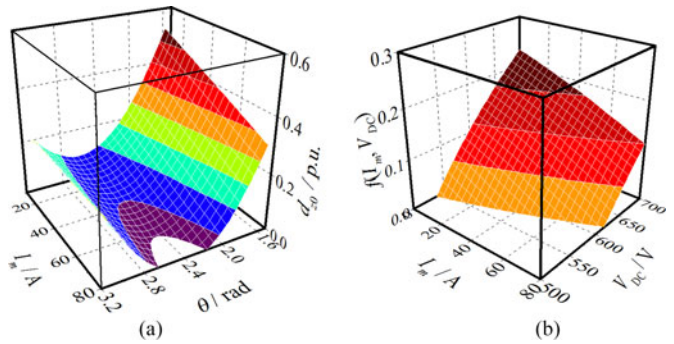

Fig. 13. (a) Value of the modulation performance evaluation function ($V_{\rm DC}$ = 600 V) versus the amplitude of and the vector angle of the converter output voltage. (b) Value of the index function versus the amplitude of and the dc-link voltage $V_{\rm DC}$.

are obtained under the condition that $V_{\rm DC}$ is set to 560 V, which is the necessary value for the linear modulation defined by the conventional modulation index *M*. The blank areas in Fig. 12 signify the over modulation region of the TPFS PWM rectifier. A conclusion can be drawn from Fig. 12 that the necessary $V_{\rm DC}$ for the linear modulation defined by the conventional modulation index *M* cannot guarantee the linear modulation of the TPFS PWM rectifier; the conventional modulation index *M* is not available for the TPFS PWM rectifier. For the TPFS PWM rectifier operating with a unity power factor, the overmodulation occurs in the second and fourth quadrants of the output voltage of the rectifier; the property of the modulation is mainly determined by the evaluation function in the sector II.

For a given dc voltage $V_{\rm DC}$, there exists a threshold value $I_{\max}$. With a smaller ac input current than the threshold value $I_{\max}$, the TPFS PWM rectifier operates in the entire linear modulation region. Otherwise, the TPFS PWM rectifier runs alternatingly in the linear modulation region and the overmodulation region. Additionally, the value of the modulation performance evaluation function is altered by the vector angle θ. To investigate the effect of the dc voltage on the modulation, the circuit parameters listed in Table IV are substituted into (51), and the dc voltage $V_{\rm DC}$ is set to 600 V. The analytical result is shown in Fig. 13(a). Compared with Fig. 12, the blank area in Fig. 13(a) is significantly reduced, and the amplitude of the ac input current threshold value $I_{\max}$ is clearly increased; the increased dc voltage is a favorable factor for the linear modulation. It is worth noting that there exists a vector angle $\theta_{\min}$ where the performance evaluation function reaches its minimum value. The positive of the minimum value of the function denotes complete linear modulation, rejecting the alternating operation between linear modulation and overmodulation.

Finally, a novel index function of the linear modulation for the TPFS PWM rectifier is built

$$f(V_{\rm DC}, I_m) = \frac{1}{2} - \frac{I_m \sin(\theta_{\min} + \phi)}{2\omega V_{\rm DC} C} - \frac{1}{V_{\rm DC}} \sqrt{3\left(E_m^2 + (\omega L I_m)^2\right)} \sin\left(\theta_{\min} - \frac{\pi}{3}\right) \tag{52}$$

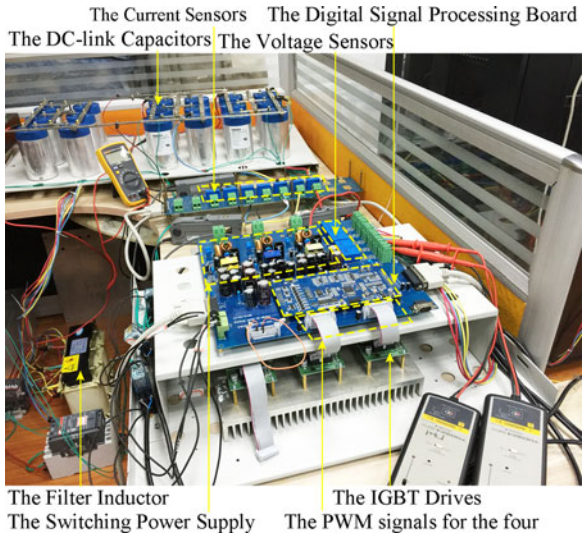

Fig. 14. 6-kVA experimental prototype.

where

$$\theta_{\min} = \pi - \arctan\left(\frac{E_m I_m + \sqrt{3}\omega C(E_m^2 + \omega^2 L^2 I_m^2)}{-\omega I_m^2 L - 3\omega C(E_m^2 + \omega^2 L^2 I_m^2)}\right). \tag{53}$$

Substituting the circuit parameters listed in Table IV and (53) into (52), the value of the index function is shown in Fig. 13(b), where I_m ranges from 0 to 80 A; in addition, $V_{\rm DC}$ ranges from 500 to 700 V. The blank area in Fig. 13(b) denotes that the rectifier runs alternatingly in the linear modulation region and the overmodulation region, generating a low-frequency harmonic current. Fig. 13(b) describes the relationship among the amplitude of ac input current, the dc voltage, and the entire linear modulation; the increased dc bus voltage is a favorable factor for linear modulation, whereas the increased amplitude of ac input current has a negative impact on the linear modulation. With the proposed index function of the linear modulation, an appropriate dc bus voltage is selected to ensure an entire linear modulation, rejecting the low-frequency harmonic current introduced by the overmodulation.

Nevertheless, as analyzed above, the lower dc voltage benefits the reduction of the ac current ripple. For better current performance, the determination of the dc voltage value should be a tradeoff between the ac current ripple and the frequency harmonic current.

VII. Experiment Verification

A 6-kVA experimental prototype has been constructed to verify the effectiveness of the proposed strategy, as shown in Fig. 14. It consists of the Semikron IGBTs (SKM200GB12V), the drivers (SKYPER 32PRO) for the IGBTs, current sensors, voltage sensors, an inductor filter, dc-side capacitors, a TMS320F2808 DSP-based signal processing board, and a switching power supply board. The parameters are listed in Table IV. A YOKOGAWA DLM2024 oscilloscope is used to measure the input currents and the output dc voltage.

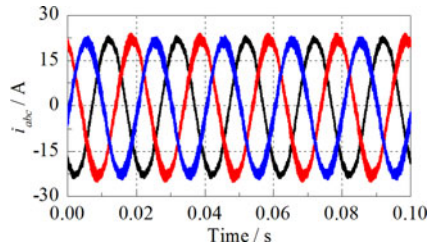

Fig. 15. Three-phase input current of the TPFS PWM rectifier using the LVSVM method.

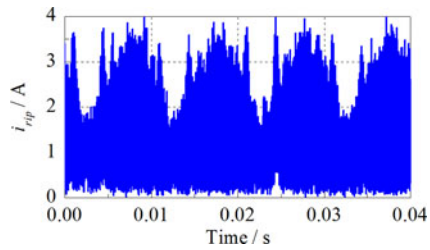

Fig. 16. Current ripple of LVSVM under the condition $V_{\mathrm{DC}} = 600$ V.

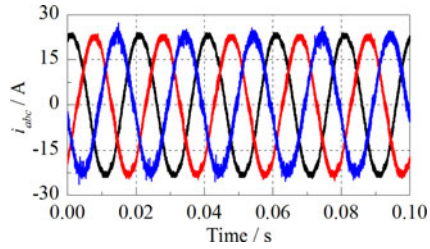

Fig. 17. Three-phase input current of the TPFS PWM rectifier using the NTSVM method.

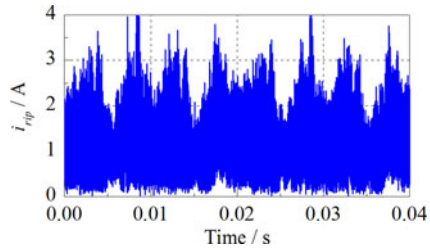

Fig. 18. Current ripple of NTSVM under the condition $V_{\mathrm{DC}} = 600$ V.

The experiment was carried out at a dc voltage of 600 V and the rated power (6 kW). Figs. 15 and 16 display the three-phase input current and current ripple of the TPFS PWM rectifier using the LVSVM method, respectively; the three-phase input current and current ripple of the TPFS PWM rectifier using the NTSVM approach are exhibited in Figs. 17 and 18; and the three-phase input current and current ripple of the TPFS PWM rectifier using the SVSVM approach are exhibited in the Figs. 19 and 20. Compared with the Figs. 16 and 18, the current ripple in the Fig. 20 is evidently small, which is consistent with the theoretical analysis in Section IV.

Fig. 21 displays the responses of the dc voltages V_{DC1} and V_{DC2} to the proposed capacitor voltage deviation control

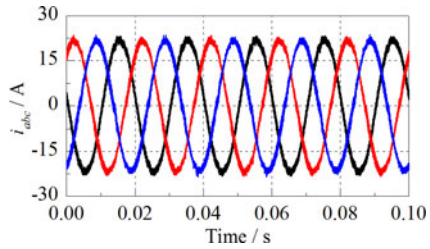

Fig. 19. Three-phase input current of the TPFS PWM rectifier using the SVSVM method.

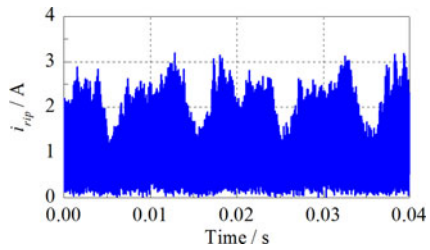

Fig. 20. Current ripple of SVSVM under the condition $V_{\mathrm{DC}} = 600$ V.

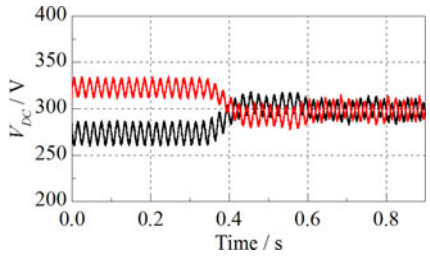

Fig. 21. DC voltage of the C_1 and C_2 of the TPFS PWM rectifier without the capacitor voltage deviation control.

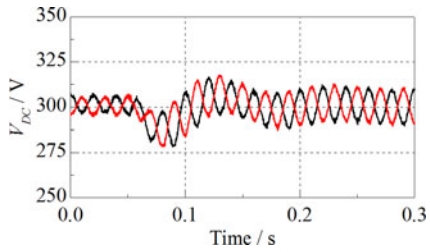

Fig. 22. Response of the dc voltage of the C_1 and C_2 to the dc load disturbance.

strategy. As shown in Fig. 21, when the proposed strategy is applied at 0.35 s, the voltage offset introduced by the initial voltage difference across the two capacitors C_1 and C_2 is eliminated at 0.4 s.

In order to validate the robustness of the proposed strategy, the rated step from 3 to 5.5 kW, is considered in this paper. The response of the dc voltage of the C_1 and C_2 and the three-phase input current to the load disturbance are shown in Figs. 22 and 23, respectively. After the step change, the capacitor voltage deviation in Fig. 22 is eliminated, and the three-phase current in Fig. 23 exhibits the symmetry. The proposed capacitor

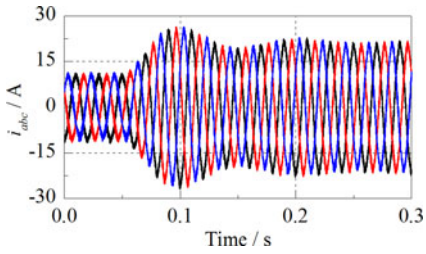

Fig. 23. Response of the three-phase input current to the dc load disturbance.

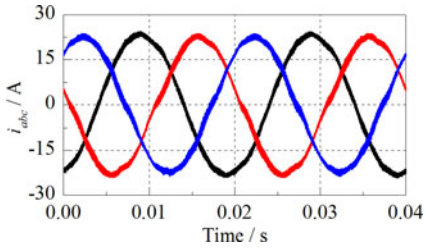

Fig. 24. Three-phase input current of the TPFS PWM rectifier under the condition $V_{\mathrm{DC}} = 560$ V.

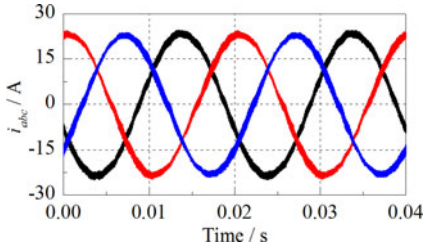

Fig. 25. Three-phase input current of the TPFS PWM rectifier under the condition $V_{\mathrm{DC}} = 600$ V.

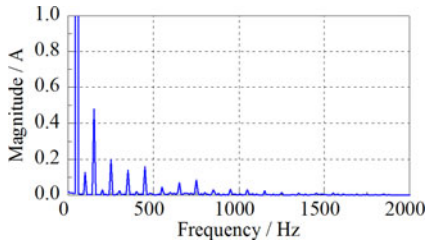

Fig. 26. FFT analysis of three-phase input current of the TPFS PWM rectifier under the condition $V_{\mathrm{DC}} = 560$ V.

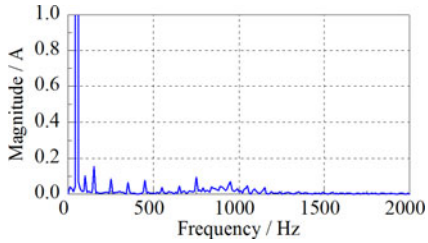

Fig. 27. FFT analysis of three-phase input current of the TPFS PWM rectifier under the condition $V_{\mathrm{DC}} = 600$ V.

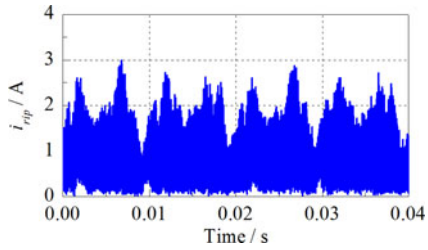

Fig. 28. Current ripple of SVSVM under the condition $V_{\mathrm{DC}} = 560$ V.

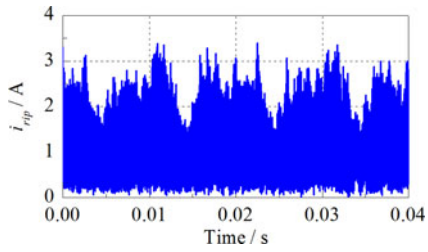

Fig. 29. Current ripple of SVSVM under the condition $V_{\mathrm{DC}} = 600$ V.

voltage deviation control strategy does not affect the control of the TPFS PWM rectifier in normal operation. It is worth noting that the amplitude of the voltage oscillation in Fig. 22 is doubled because of the double amplitude of ac input current I_m, which is consistent with the above theoretical analysis.

To validate the reliability and accuracy of the proposed index function of the linear modulation, comparisons have been made between TPFS PWM rectifiers with a V_{DC} of 560 V and TPFS PWM rectifiers with a V_{DC} of 600 V, where both of the TPFS PWM rectifiers have the rated power $P = 6$ kW and regulated by identical current and voltage controllers. According to the above analysis, when V_{DC} is set to 560 V, which is the necessary value for the linear modulation defined by the conventional modulation index *M*, the TPFS rectifier operates alternatingly in the linear modulation region and the overmodulation region, introducing the low-frequency harmonic current, as shown in Figs. 24 and 26. When the dc voltage is set to 600 V, the necessary value defined by the proposed index function of the linear modulation, the TPFS rectifier runs entirely in the linear modulation region. Therefore, in Figs. 25 and 27, the low-frequency harmonic current and the distortion of the three-phase input current are rejected, which in turn demonstrates the usefulness and accuracy of the proposed index function of the linear modulation.

In addition, as analyzed above, the RMS values of the current ripple increase with the increasing dc voltage. Thus, the current ripple in Fig. 28 is smaller than the current ripple in Fig. 29.

The TPFS PWM rectifier is also tested under unity power factor mode and inductive load mode. The i_q^* is set to 0 A to obtain the unity power factor of grid side, and is set to -10A (power factor is set to 0.8) for inductive load mode. As shown in Figs. 30 and 31, the rectifier operates well in both modes, providing a valid evidence for the robustness of the proposed model and controller design method.

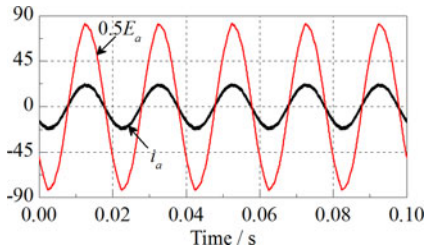

Fig. 30. Voltage and current of the rectifier under a unity power factor mode ($V_{\rm DC} = 600$ V).

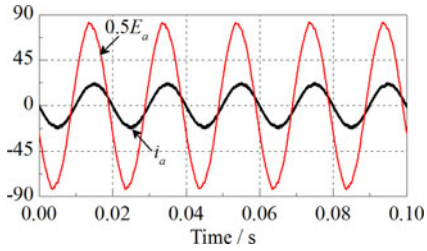

Fig. 31. Voltage and current of the rectifier under an inductive load mode ($V_{\rm DC} = 600$ V).

VIII. Conclusion

Three space vector pulse width modulation methods using the different equivalent zero voltage vectors are developed, where sector identification and the trigonometric functions are not required. Then, a high-frequency model for the current ripple analysis is proposed, and the effects of three SVM approaches on the ac current ripple are analyzed. The analytical expressions are derived in the time domain, which consist of simple equations. Using the proposed equation, it is convenient to investigate the ac current ripple RMS of various SVM approaches. The analytical results reveal that the ac current ripple RMS of the TPFS using the SVSVM is smaller than that of the TPFS adopting the LVSVM and NTSVM modulation schemes. Additionally, a conclusion can be drawn from the analytical results that the higher dc voltage is an unfavorable factor for the current ripple reduction.

Furthermore, using the SVSVM approach, the ac component of the output voltage in the *dq* synchronous frame is eliminated, and a low-frequency control-oriented model in the *dq* synchronous frame is presented to facilitate the controller design. The proposed model-based controller provides the TPFS rectifier excellent steady-state performance and satisfactory dynamic response. To guarantee the stable operation of the TPFS rectifier, a control strategy adopting the proportional controller is proposed to eliminate the capacitor voltage deviation. Meanwhile, the dual-loop control of the TPFS PWM rectifier is not affected by the capacitor voltage deviation control loop when the capacitor voltage deviation is eliminated.

Moreover, a modulation evaluation function $f(V_{\rm DC}, I_m, \theta)$ is proposed to evaluate the modulation properties of the TPFS rectifier, and the proposed modulation evaluation function reveals that the conventional modulation index M is not available to evaluate the modulation properties of the TPFS rectifier. Then, a linear modulation index function is developed to illustrate the relationship among the linear modulation, the dc-link voltage, and the AC input current. Finally, a significant conclusion can be drawn from the analytical and experimental results that the ac current ripple and the linear modulation both should be taken into account when selecting the dc bus voltage of the TPFS rectifier. Experimental results verify that excellent current performance of the TPFS PWM rectifier is achieved with the comprehensive considerations of the modeling, modulation, and control strategy.

References

[1] B. Parkhideh and S. Bhattacharya, "Vector-controlled voltage-source-converter-based transmission under grid disturbances," *IEEE Trans. Power Electron.*, vol. 28, no. 2, pp. 661–672, Feb. 2013.

[2] S. Yoon, H. Oh, and S. Choi, "Controller design and implementation of indirect current control based utility-interactive inverter system," *IEEE Trans. Power Electron.*, vol. 28, no. 1, pp. 26–30, Jan. 2013.

[3] J. B. Hu and Z. Q. Zhu, "Improved voltage-vector sequences on dead-beat predictive direct power control of reversible three-phase grid-connected voltage-source converters," *IEEE Trans. Power Electron.*, vol. 28, no. 1, pp. 254–267, Jan. 2013.

[4] T. Messo, J. Jokipii, J. Puukko, and T. Suntio, "Determining the value of DC-link capacitance to ensure stable operation of a three-phase photovoltaic inverter," *IEEE Trans. Power Electron.*, vol. 29, no. 2, pp. 665–673, Feb. 2014.

[5] S. C. Shin, H. J. Lee, Y. H. Kim, J. H. Lee, and C. Y. Won, "Transient response improvement at startup of a three-phase AC/DC converter for a DC distribution system in commercial facilities," *IEEE Trans. Power Electron.*, vol. 29, no. 12, pp. 6742–6753, Dec. 2014.

[6] T. D. Nguyen, N. Patin, and G. Friedrich, "Extended double carrier PWM strategy dedicated to RMS current reduction in DC link capacitors of three-phase inverters," *IEEE Trans. Power Electron.*, vol. 29, no. 1, pp. 396–406, Jan. 2014.

[7] Z. Liu, J. J. Liu, and Y. L. Zhao, "A unified control strategy for three-phase inverter in distributed generation," *IEEE Trans. Power Electron.*, vol. 29, no. 3, pp. 1176–1191, Mar. 2014.

[8] Y. T. Song and B. S. Wang, "Survey on reliability of power electronic systems," *IEEE Trans. Power Electron.*, vol. 28, no. 1, pp. 591–604, Jan. 2013.

[9] B. Mirafzal, "Survey of fault-tolerance techniques for three-phase voltage source inverters," *IEEE Trans. Ind. Electron.*, vol. 61, no. 10, pp. 5192–5202, Oct. 2014.

[10] H. W. Van Der Broeck and J. D. Van Wyk, "A comparative investigation of a three-phase induction machine drive with a component minimized voltage-fed inverter under different control options," *IEEE Trans. Ind. Appl.*, vol. IA-20, no. 2, pp. 309–320, Mar. 1984.

[11] F. Blaabjerg, S. Freysson, H. H. Hansen, and S. Hansen, "A new optimized space-vector modulation strategy for a component-minimized voltage source inverter," *IEEE Trans. Power Electron.*, vol. 12, no. 4, pp. 704–714, Jul. 1997.

[12] M. Beltrao De Rossiter Correa, C. B. Jacobina, E. R. Cabral da Silva, and A. M. N. Lima, "A general PWM strategy for four-switch three-phase inverters," *IEEE Trans. Power Electron.*, vol. 21, no. 6, pp. 1618–1627, Nov. 2006.

[13] W. Wen, L. An, X. Xianyong, F. Lu, M. C. Thuyen, and L. Zhou, "Space vector pulse-width modulation algorithm and DC-side voltage control strategy of three-phase four-switch active power filters," *IET Power Electron.*, vol. 6, no. 1, pp. 125–135, 2013.

[14] R. Wang, J. Zhao, and Y. Liu, "A comprehensive investigation of four-switch three-phase voltage source inverter based on double Fourier integral analysis," *IEEE Trans. Power Electron.*, vol. 26, no. 10, pp. 2774–2787, Oct. 2011.

[15] J. Klima, J. Skramlik, and V. Valouch, "An analytical modeling of three-phase four-switch PWM rectifier under unbalanced supply conditions," *IEEE Trans. Circuits Syst. II, Exp. Briefs*, vol. 54, no. 12, pp. 1155–1159, Dec. 2007.

[16] S. Ounie and M. R. Zolghadri, "Space vector modulation for four-switch rectifier with compensating the effect of capacitors voltage ripple," presented at the Int. Conf. Electric Power Energy Conversion Systems., Sharjah, UAE, 2009.

[17] G. L. Peters, G. A. Covic, and J. T. Boys, "Eliminating output distortion in four-switch inverters with three-phase loads," in *Proc. IEE Electr. Power Appl.*, vol. 145, no. 4, pp. 326–332, Jul. 1998.

[18] W. Sae-Kok, D. M. Grant, and B. W. Williams, "System reconfiguration under open-switch faults in a doubly fed induction machine," *IET Renew. Power Gener.*, vol. 4, no. 5, pp. 458–470, Sep. 2010.
[19] Q. T. An, L. Sun, K. Zhao, and T. M. Jahns, "Scalar PWM algorithms for four-switch three-phase inverters," *Electron. Lett.*, vol. 46, pp. 900–902, 2010.
[20] F. Blaabjerg, D. O. Neacsu, and J. K. Pedersen, "Adaptive SVM to compensate DC-link voltage ripple for four-switch three-phase voltage-source inverters," *IEEE Trans. Power Electron.*, vol. 14, no. 4, pp. 743–752, Jul. 1999.
[21] M. Monfared, H. Rastegar, and H. M. Kojabadi, "Overview of modulation techniques for the four-switch converter topology," in *Proc. IEEE 2nd Int. Power Energy Conf.*, Johor Bahru, Malaysia, 2008, pp. 803–807.
[22] J. J. Shieh, C. T. Pan, and Z. J. Cuey, "Modelling and design of a reversible three-phase switching mode rectifier," in *Proc. IEE Electr. Power Appl.*, vol. 144, no. 6, pp. 389–396, Nov. 1997.
[23] M. C. Jiang, "A novel power electronics bidirectional interface," *IEEE Trans. Aerosp. Electron. Syst.*, vol. 33, no. 4, pp. 1132–1141, Oct. 1997.
[24] Y. K. Lo, H. J. Chiu, and W. T. Li, "A reduced hysteresis controller for a four-switch three-phase bidirectional power electronics interface," *IEEE Trans. Ind. Electron.*, vol. 46, no. 4, pp. 864–866, Aug. 1999.
[25] N. M. A. Freire and A. J. Marques Cardoso, "A fault-tolerant direct controlled PMSG drive for wind energy conversion systems," *IEEE Trans. Ind. Electron.*, vol. 61, no. 2, pp. 821–834, Feb. 2014.
[26] T. S. Lee and J. H. Liu, "Modeling and control of a three-phase four-switch PWM voltage-source rectifier in d-q synchronous frame," *IEEE Trans. Power Electron.*, vol. 26, no. 9, pp. 2476–2489, Sep. 2011.
[27] Y. Gu, D. L. Zhang, and Z. Y. Zhao, "Input/output current ripple cancellation and RHP zero elimination in a boost converter using an integrated magnetic technique," *IEEE Trans. Power Electron.*, vol. 30, no. 2, pp. 747–756, Feb. 2015.
[28] X. H. Liu, H. Li, and Z. Wang, "A fuel cell power conditioning system with low-frequency ripple-free input current using a control-oriented power pulsation decoupling strategy," *IEEE Trans. Power Electron.*, vol. 29, no. 1, pp. 159–169, Jan. 2014.
[29] J. Yang and F. C. Lee, "LCL filter design and inductor ripple analysis for 3-level NPC grid interface converter," in *Proc. Energy Convers. Congr. Expo*, Pittsburgh, PA, USA, 2014, pp. 1911–1918.
[30] J. H. Wang, B. J. Ji, X. Q. Lu, X. Deng, F. H. Zhang, and C. Y. Gong, "Steady-state and dynamic input current low-frequency ripple evaluation and reduction in two-stage single-phase inverters with back current gain model," *IEEE Trans. Power Electron.*, vol. 29, no. 8, pp. 4247–4260, Aug. 2014.
[31] D. Jiang and F. Wang, "A general current ripple prediction method for the multiphase voltage source converter," *IEEE Trans. Power Electron.*, vol. 29, no. 6, pp. 2643–2648, Jun. 2014.
[32] K. Basu, A. K. Sahoo, V. Chandrasekaran, and N. Mohan, "Grid-side AC line filter design of a current source rectifier with analytical estimation of input current ripple," *IEEE Trans. Power Electron.*, vol. 29, no. 12, pp. 6394–6405, Dec. 2014.
[33] D. Jiang and F. Wang, "Variable switching frequency PWM for three-phase converters based on current ripple prediction," *IEEE Trans. Power Electron.*, vol. 28, no. 11, pp. 4951–4961, Nov. 2013.
[34] V. Blasko and V. Kaura, "A new mathematical model and control of a three-phase AC-DC voltage source converter," *IEEE Trans. Power Electron.*, vol. 12, no. 1, pp. 116–123, Jan. 1997.
[35] Y. Bo, R. Oruganti, S. K. Panda, and A. K. S. Bhat, "A simple single-input-single-output (SISO) model for a three-phase PWM rectifier," *IEEE Trans. Power Electron.*, vol. 24, no. 3, pp. 620–631, Mar. 2009.
[36] A. K. Gupta and A. M. Khambadkone, "A general space vector PWM algorithm for multilevel inverters, including operation in overmodulation range," *IEEE Trans. Power Electron.*, vol. 22, no. 2, pp. 517–526, Mar. 2007.
[37] A. Tripathi, A. M. Khambadkone, and S. K. Panda, "Dynamic control of torque in overmodulation and in the field weakening region," *IEEE Trans. Power Electron.*, vol. 21, no. 4, pp. 1091–1098, Jul. 2006.
[38] D. Casadei, G. Serra, A. Tani, and L. Zarri, "Theoretical and experimental analysis for the RMS current ripple minimization in induction motor drives controlled by SVM technique," *IEEE Trans. Ind. Electron.*, vol. 51, no. 5, pp. 1056–1065, Oct. 2004.
[39] Y. Bo, R. Oruganti, S. K. Panda, and A. K. S. Bhat, "Experimental verification of a dual single-input single-output model of a three-phase boost-type PWM rectifier," in *Proc. Ind. Electron. Soc. Conf.*, Raleigh, NC, USA, 2005, pp. 1030–1035.
[40] R. Teodorescu and F. Blaabjerg, "Flexible control of small wind turbines with grid failure detection operating in stand-alone and grid-connected mode," *IEEE Trans. Power Electron.*, vol. 19, no. 5, pp. 1323–1332, Sep. 2004.

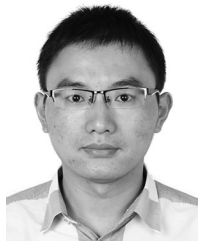

Zhiyong Zeng received the B.Sc. and M.Sc. degrees in electrical engineering from the Anhui University of Science and Technology, Huainan, China, in 2006 and 2009, respectively. He is currently working toward the Ph.D. degree at Zhejiang University, Hangzhou, China.

His current research interests include modeling, modulation, and control of grid-connected power converters and fault-tolerant power converters implemented in renewable energy and distributed generation systems.

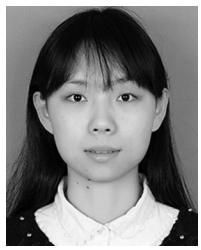

Weiyi Zheng received the B.Sc. degree in electrical engineering from the Zhejiang University of Technology, Hangzhou, China, in 2013. She is currently working toward the M.Sc. degree at Zhejiang University, Hangzhou.

Her current research interest includes fault-tolerant grid-connected power converter implemented in wind energy conversion systems.

Rongxiang Zhao received the B.Sc., M.Sc., and Ph.D. degrees in electrical engineering from Zhejiang University, Hangzhou, China, in 1984, 1987, and 1991, respectively.

He became a Faculty Member at Zhejiang University in 1991, and promoted to an Associate Professor in December 1994. Since 1997, he has been a Full Professor at the College of Electrical Engineering, Zhejiang University, where he was the Vice Dean with the College of Electrical Engineering. He is currently the Director at the National Engineering Research Center for Applied Power Electronics of China, Zhejiang University, where he focuses on the integration of enterprises, universities, and research institutes in power electronics applications, such as induction heating, electric vehicle drives, microgrids, etc. He has published more than 60 technical papers, and holds 16 patents. His current research interests include renewable energy generation, motor control, and energy storage and its applications.

Dr. Zhao received the six Scientific and Technological Achievements Awards from the Zhejiang Provincial Government and one Science and Technology Progress Award from the State Educational Ministry of China.

Chong Zhu received the B.Sc. degree in electrical engineering from the China University of Mining and Technology, Xuzhou, China, in 2010. He is currently working toward the Ph.D. degree in electrical engineering at Zhejiang University, Hangzhou, China.

His research interests include modulation techniques and fault-tolerant control of power converters.

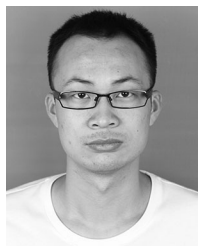

Qingwei Yuan received the B.Sc. degree from Hunan University, Changsha, China, in 2010. He is currently working toward the Ph.D. degree at Zhejiang University, Hangzhou, China.

His current research interests include direct torque control of interior permanent magnet synchronous motor and direct-drive wind energy conversion system.